Postprint of: Lachowicz J., Rucka M., A novel heterogeneous model of concrete for numerical modelling of ground penetrating radar, Construction and Building Materials, vol. 227 (2019), DOI: 10.1016/j.conbuildmat.2019.116703

A novel heterogeneous model of concrete for numerical modelling of ground penetrating radar

Jacek Lachowicz[1], Magdalena Rucka[2]*

[1]*FORT POLSKA sp. z o.o.*
ul. Nowotoruńska 8, 85-840 Bydgoszcz
email: jacek.lachowicz@fort.pl

[2]*Department of Mechanics of Materials and Structures*
Faculty of Civil and Environmental Engineering
Gdańsk University of Technology
ul. Narutowicza 11/12, 80-233 Gdańsk, Poland
email: mrucka@pg.edu.pl or magdalena.rucka@pg.edu.pl
**corresponding author*

Abstract

The ground penetrating radar (GPR) method has increasingly been applied in the non-destructive testing of reinforced concrete structures. The most common approach to the modelling of radar waves is to consider concrete as a homogeneous material. This paper proposes a novel, heterogeneous, numerical model of concrete for exhaustive interpretation of GPR data. An algorithm for determining the substitute values of the material constants of concrete is developed, based on the modified complex refractive index method. Experimental surveys and numerical simulations are conducted on a concrete laboratory sample with a controlled degree of saturation, and on a real concrete slab with two different degrees of saturation. The results indicate that the proposed model is fully capable of realistic finite-difference time-domain modelling of concrete for ground penetrating radar diagnostics of civil engineering structures with changing water content.

Keywords

Ground penetrating radar; non-destructive testing; finite-difference time-domain modelling; heterogeneous model; concrete, dielectric property

1. Introduction

Ground penetrating radar (GPR) is used in a wide range of applications aimed at diagnostics, evaluation, and the maintenance of civil engineering structures [1,2]. The GPR method has proved particularly useful for assessing the condition of structures made from reinforced concrete. In such structures, radar surveys focus on two main areas: inspection of the reinforcing bars, and inspection of the concrete. Previous studies have indicated a significant potential for the GPR technique in the identification of the number, position, and distribution of the rebars in concrete elements [3–5]. The research also focused on the identification of the diameter of the steel bars [6,7], influence of the bar spacing on the GPR maps [8], inspection of the different arrangements of bars [9], and monitoring of the bar corrosion [10,11]. For the precise and automatic detection of reinforcing bars, different models of hyperbolic signatures have been developed, including the simplest model reducing a bar to a point [12,13], the model considering a bar as a cylindrical object having nonzero radius [14–17], and the model considering an actual bar radius and distance between the transmitting and receiving antennas [18,19]. GPR applications for the inspection of concrete have concerned detection of the following: cracks and voids [20], influence of chloride on the permittivity of the concrete [21], evaluation of the water content in the concrete [22–25], characterisation of the concrete mechanical properties in terms of dielectric properties [26], monitoring of the concrete at high temperature [27], and hydration monitoring of young concrete [28].

In recent years, the numerical modelling of electromagnetic wave propagation using a finite-difference time-domain (FDTD) method has become a powerful tool for the exhaustive interpretation of GPR data. In previous studies concerning numerical modelling aimed at supporting GPR diagnostics in civil engineering structures, materials such as concrete [9,29–31], stone [32], and bricks [33,34] have been considered as homogeneous, which was frequently a sufficient simplification. Currently, there is an increasing interest in the development of more precise, heterogeneous models of materials, where the electromagnetic field propagates. The majority of the research to date has concentrated on realistic FDTD modelling of soil, including soil's inhomogeneity and the roughness of the soil's surface ([35,36]). However, to the best of the authors' knowledge, there is no common method for modelling concrete as a heterogeneous material.

This study aims to simulate the GPR surveys in a heterogeneous and porous material (concrete) more realistically. The objective of this paper is to propose a novel numerical

heterogeneous model of concrete for FDTD simulations. First, an algorithm for determining the substitute values of the dielectric properties is developed. Then, it is validated on a laboratory concrete specimen with a controlled saturation level. Finally, the proposed model is used to study the influence of the water content contained in a bridge deck.

2. Proposed heterogeneous model of concrete

The simplest model of a heterogeneous material considering the effective dielectric permittivity of a medium can be described by the complex refractive index method (CRIM). Owing to its simplicity and despite its lack of theoretical foundations, it is widely used to describe rocks, soil, and concrete. The CRIM assumes that the effective permittivity of a mixture can be expressed as the volume average of the effective permittivity of the components [37]:

$$\sqrt{\varepsilon_e} = (1-\Phi)\sqrt{\varepsilon_m} + (1-S)\Phi\sqrt{\varepsilon_a} + \Phi S\sqrt{\varepsilon_w}\,, \tag{1}$$

where

ε_e – relative effective permittivity of concrete mixture,

ε_m – relative permittivity of the solid phase (concrete solid),

ε_a – relative permittivity of the gas phase (air),

ε_w – relative permittivity of the liquid phase (water),

Φ – porosity of concrete, and

S – degree of pore saturation.

In this paper, we propose an original heterogeneous numerical model of concrete, where the distribution of the individual concrete components is pseudorandom. A Python script was written to generate a pseudorandom position of the individual components of the concrete, considering the percentage distribution of the fractions and their dimensions. In the model, any graining curve created from a fraction between 1 and 32 mm can be used. Moreover, different dielectric properties can be assigned to each fraction. The script was implemented in the gprMax [38,39] input file. To begin, a computational area is defined where a heterogeneous mixture is to be created. Then, the percentage composition of the individual concrete components with the graining curve is specified (Figure 1a). In the next step, the values of the material constants are assigned to each defined component of the mixture. The definition of the other calculation parameters remains unchanged with respect to the homogeneous models. Finally, the geometry of the heterogeneous mixture is formed with the pseudorandom distribution of the individual concrete components (Figure 1b).

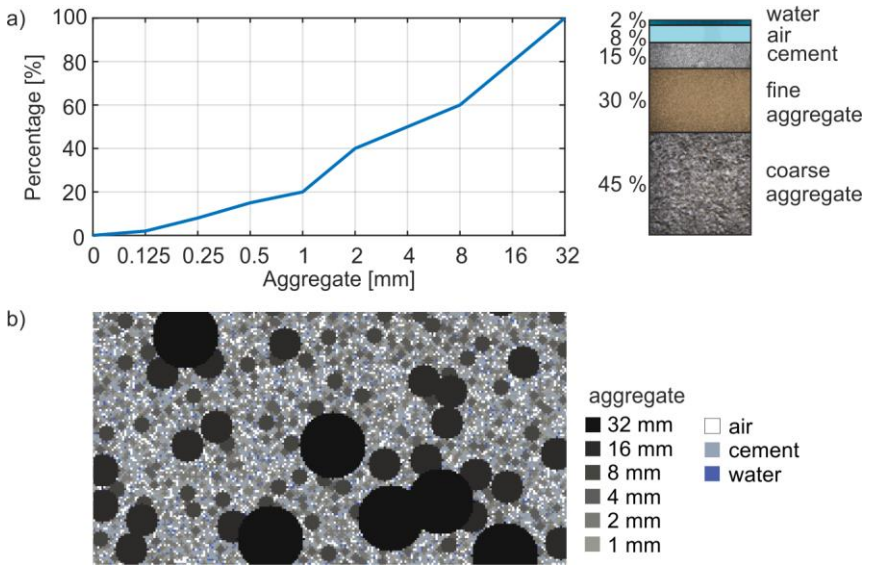

Figure 1. Developed heterogeneous numerical model of concrete: a) example of concrete composition and grain-size distribution curve and b) visualisation of distribution of individual fractions

It is proposed that the material constants attributed to the individual components should be described in accordance with the CRIM. Therefore, the creation of the heterogeneous numerical model of concrete requires the identification of material parameters (i.e. the dielectric permittivity and conductivity) of a tested concrete element for different degrees of saturation. The algorithm for determining the substitute values of the material constants for the numerical model is presented below. It includes the following steps:

Step 1. **Determination of volumetric absorption** N_V **and porosity** Φ of a sample according to relations:

$$N_V = \frac{m_{100\%} - m_{0\%}}{V} \cdot 100\%, \tag{2}$$

$$\Phi = \frac{\rho_m - \rho_V}{\rho_m} \cdot 100\%, \tag{3}$$

where

$m_{100\%}$ – mass of a saturated sample,

$m_{0\%}$ – mass of a sample dried to a constant mass,

V – volume of a sample,

ρ_V – density, and

ρ_m – density of the solid phase.

Step 2. **Execution of GPR measurements for different levels of saturation** (Step 2 must be repeated for at least two different degrees of saturation):

2.1. Determination of the degree of saturation S_V of a concrete element according to the formula:

$$S_V = \frac{w}{N_V} \cdot 100\%, \tag{4}$$

$$w = \frac{m_{X\%} - m_{0\%}}{m_{0\%}} \cdot 100\%, \tag{5}$$

where

w – moisture of a concrete element and

$m_{X\%}$ – mass of a concrete element at a given degree of saturation.

2.2. Execution of GPR measurements and determination of the velocity of electromagnetic waves *v*.

2.3. Determination of the effective value of dielectric permittivity:

$$\varepsilon_e = \frac{c^2}{v^2}. \tag{6}$$

Step 3. **Approximation of the measured data using the CRIM** assuming that the material constants of the liquid and gas phases are known ($\varepsilon_a = 1$, $\varepsilon_w = 79.1 + i8.6$). Because not all air pores must be filled with water, we propose a modification to Eq. (1), by introducing the volumetric absorption and degree of saturation. Consequently, an equation called a modified CRIM is obtained:

$$\sqrt{\varepsilon_e} = (1-\Phi)\sqrt{\varepsilon_m} + \left(\Phi - N_V S_V\right)\sqrt{\varepsilon_a} + N_V S_V \sqrt{\varepsilon_w}, \tag{7}$$

from which the value of the solid phase permeability ε_m can be calculated.

Step 4. **Determination of substitute values of the permittivity**. Because in the numerical model the effective permittivity value is the weighted average of the individual components, we propose an equation, called a numerical CRIM:

$$\varepsilon_e = (1-\Phi)\varepsilon_{ms} + \left(\Phi - N_V S_V\right)\varepsilon_a + N_V S_V \varepsilon_{ws}. \tag{8}$$

Equation (8), assuming that the permittivity of the gas phase cannot change ($\varepsilon_a = 1$), enables a nonlinear approximation for the substitute dielectric permittivity parameters of the liquid and solid phases (i.e. ε_{ws} and ε_{ms}).

Step 5. **Determination of the substitute value of the dielectric conductivity** to simulate the damping properties of the material. For this purpose, the following equation can be used [40]:

$$\sigma = \omega \cdot \varepsilon'', \tag{9}$$

where ε" denotes the imaginary part of ε.

It should be noted that the algorithm for determining the substitute values of the material constants described above is an approximate method. The approximations are performed at each stage, starting from the determination of the density and porosity, ending with the assumptions regarding the permittivity of the liquid phase. However, as indicated by the investigations performed in this work, the proposed model can be considered significantly closer to reality than the homogeneous model of concrete for GPR purposes.

In the case of diagnostic tests performed on existing structures, the information regarding the components of the concrete is typically not known. In such cases, reasonable assumptions of the volumetric absorption and porosity values must be made. In the authors' opinion, the error caused by these assumptions does not exceed 10%. Moreover, knowledge and experience in the analysis of the concrete mixes can reduce the error to a minimum. The error can be also minimised by the application of destructive methods and laboratory tests of samples from the investigated structures.

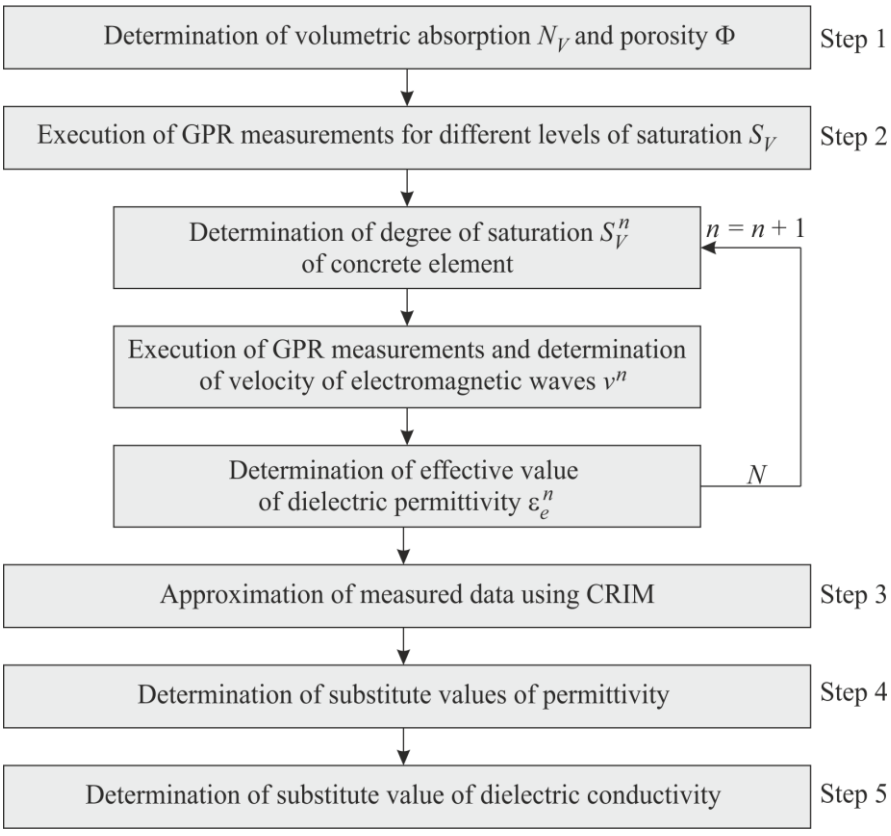

Figure 2. Flow chart illustrating proposed algorithm for determining substitute values of material constants

3. GPR investigations on reinforced concrete specimen

3.1. Description of specimen

GPR investigations were performed on a reinforced concrete sample with external dimensions of 80 cm × 10 cm × 15 cm. A total of 10 steel bars were embedded in the specimen: 3 bars with a diameter of 14 mm, 3 bars with a diameter of 12 mm, and 4 bars with a diameter of 6 mm. One occurrence of transverse damage was included in the form of a rectangular notch 20 mm wide and 40 mm high. The sample was composed of concrete of class C20/25 including the following ingredients: cement type BV 42.5 (210 kg/m^3), aggregate 0/2 mm (730 kg/m^3), aggregate 2/8 mm (540 kg/m^3), aggregate 8/16 mm (640 kg/m^3), and water (165 kg/m^3). A photograph of the reinforced concrete specimen with dimensions measured after it was completed is presented in Figure 3.

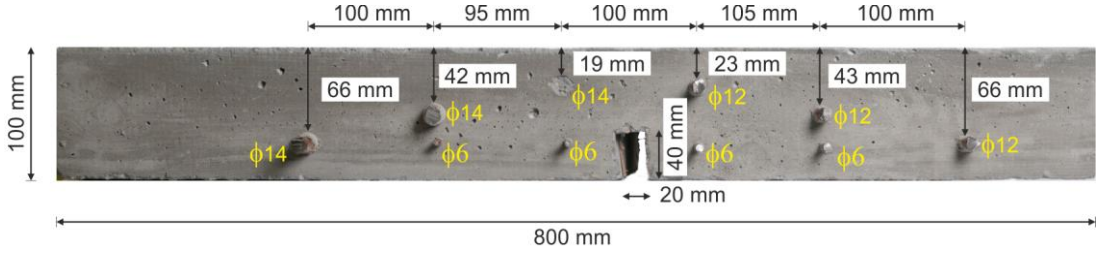

Figure 3. Photograph of reinforced concrete specimen with dimensions and positions of steel bars

3.2. GPR surveys

GPR measurements were conducted using the Aladdin system manufactured by IDS GeoRadar (Pisa, Italy) with an antenna unit operating with a frequency of 2 GHz. The distance between the transmitting and receiving antennas was 6 cm. The GPR data were collected using K2 FastWave software (manufacturer: IDS GeoRadar, version: 2.02.000) and processed in GRED HD software (manufacturer: IDS GeoRadar, version: 01.06.002). Two measurements were recorded each time (Figure 3). The first (A-scan) was conducted over the unreinforced part of the specimen to estimate the wave propagation velocity in the concrete. The second was the B-scan, which was performed along the specimen length to analyse the effect of moisture on the radargram. The survey parameters were: 6 ns range, 512 samples per scan, and 4 mm step.

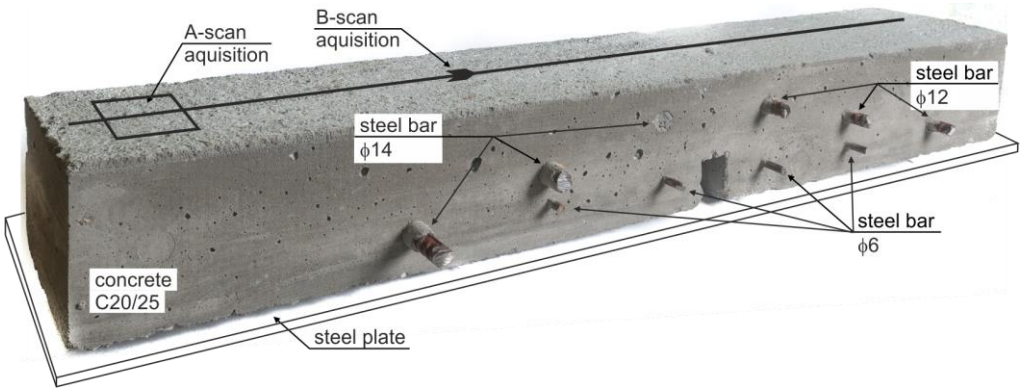

Figure 4. Reinforced concrete specimen on steel plate during GPR measurements

3.3. Identification of material properties

Experimental measurements were performed to determine the dielectric parameters of the concrete. The specimen was dried to a constant mass, weighed, and then completely immersed in water for four days and weighed again. In this manner, the volumetric absorption was determined as N_V = 10%. The porosity was determined in an approximate fashion, using the standard concrete density (2800 kg/m^3), obtaining a value equal to Φ = 23%. Then, the specimen was subjected to drying and GPR measurements were recorded successively, monitoring the decrease in the specimen weight. During GPR surveys, the concrete specimen was placed on a steel plate to determine accurately the reflection of the electromagnetic waves from the bottom of the sample. Measurements were recorded until the sample was fully dry. Table 1 presents the change of the specimen mass and degree of saturation, measured from the moment of removing the specimen from the water.

Table 1. Change of specimen mass and degree of saturation with time of drying

Time t [h]	**Mass of specimen** $m_{X\%}$ [kg]	**Degree of saturation** S_V [%]
0	27.28	100.0%
12	27.15	89.5%
25	27.05	81.0%
35	26.97	74.3%
47	26.91	69.2%
60	26.87	65.8%
72	26.82	61.6%
83	26.80	59.5%
98	26.77	57.4%
121	26.74	54.9%
145	26.72	53.2%
175	26.69	50.6%
238	26.66	48.1%
323	26.64	46.0%
540	26.60	43.0%
1271	26.54	38.0%
2201	26.49	33.8%
4259	26.43	28.7%
4269	26.34	21.1%

4288	26.25	13.1%
4381	26.17	6.8%
4456	26.09	0.0%

Figure 5 displays selected A-scans for different degrees of saturation with marked reflection amplitude from the steel plate. It can be observed that the amount of the reflected energy decreased with the increase of the degree of saturation. The relationship between the amplitude of the reflected signal and degree of saturation for all conducted GPR surveys is plotted in Figure 6. The decrease of the wave amplitude with the increase of the saturation level can be observed.

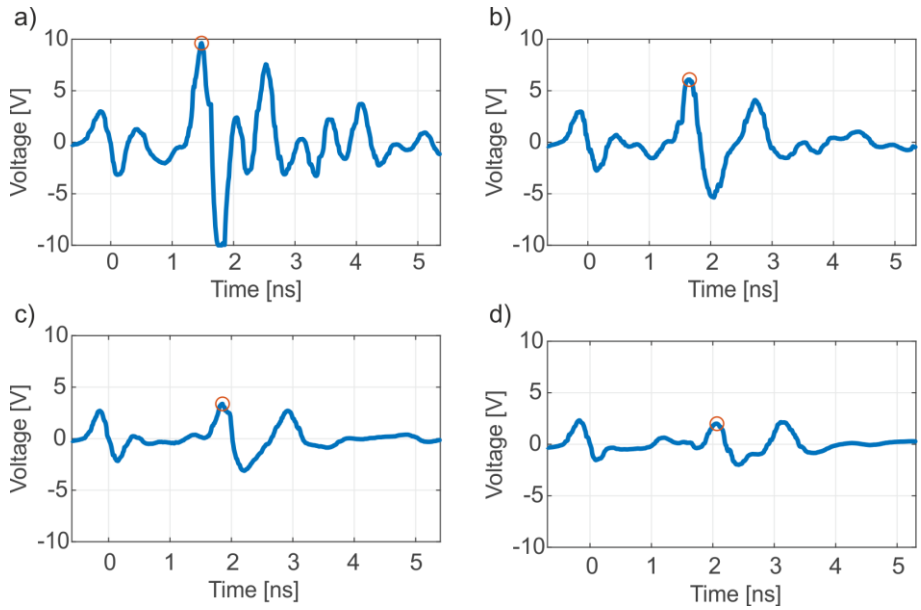

Figure 5. Selected A-scans with marked reflection amplitude for different degrees of saturation: a) 0%, b) 33.76%, c) 65.82%, and d) 100%

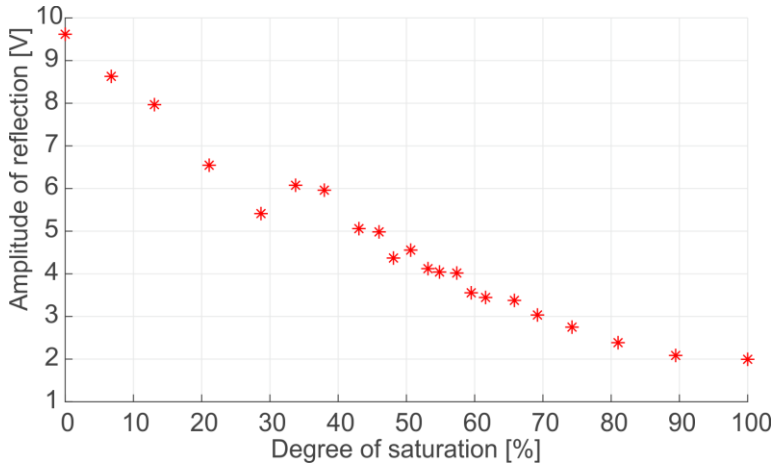

Figure 6. Relationship between amplitude of reflected signal and degree of saturation

Based on the registered A-scans, the time of the wave reflection from the steel plate was established using the first peak with a positive value (see Figure 4). Then, the velocity of the electromagnetic wave in concrete was determined based on the known height of the specimen

("depth to known reflector method" [19]), and the value of the effective permittivity was calculated. Figure 7 illustrates the relationship between the permittivity and degree of saturation. Experimental data are plotted as red circles. It is clearly visible that the permittivity value increases as the degree of saturation increases.

In the next step, on the basis of the measured permittivity values, the modified CRIM was applied according to Eq. (7) using the Levenberg–Marquardt method [41]. It was assumed that the material constants of the liquid and gas phases were known ($\varepsilon_a = 1$, $\varepsilon_w = 79.1 + i8.6$). Based on the CRIM curve fitting process (blue line in Figure 7), the dielectric permittivity for the solid phase was obtained as $\varepsilon_m = 6.21$.

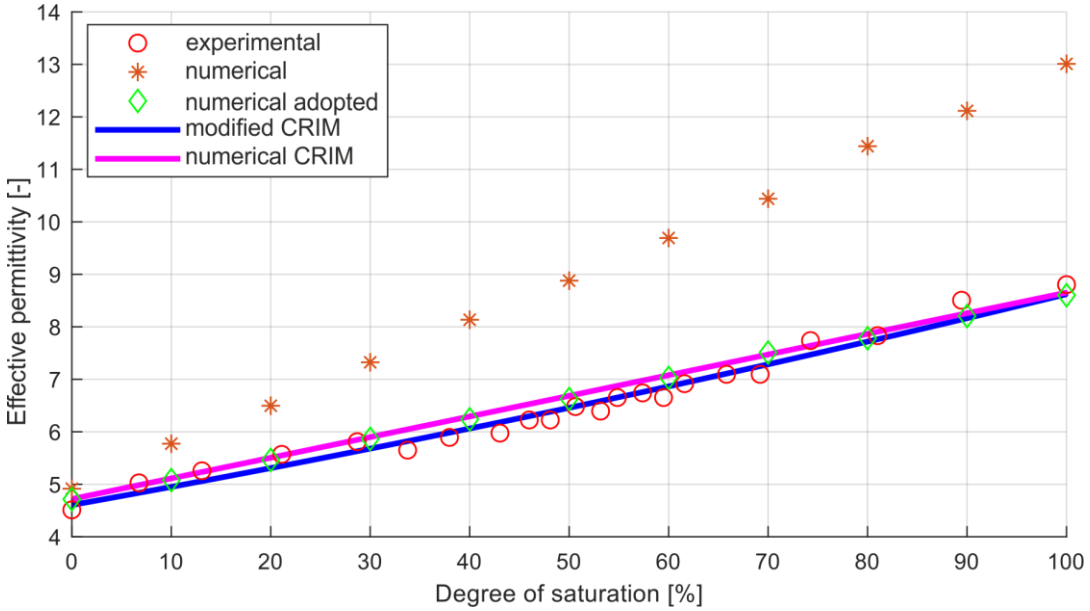

Figure 7. Relationship between effective permittivity and degree of saturation for tested concrete specimen

3.4. Determination of substitute values of material properties for numerical modelling

To verify the heterogeneous numerical model of concrete, two-dimensional (2-D) FDTD simulations were performed using gprMax [38,39,42]. A part of the concrete specimen where there were no reinforcing bars was analysed. The area of the calculation model was 25 cm × 20 cm and included a 5 cm thick layer of air, the concrete sample of dimensions 25 cm × 10 cm, and the steel plate to increase the amplitude of the reflected signal. Eleven numerical models were generated with varying degrees of concrete saturation from 0% to 100%, with a step of 10%. The porosity of the concrete was assumed to be 23% and the volumetric absorption 10%, according to the experimental results. The geometry of the calculation model for the 0% degree of saturation is displayed in Figure 8.

The excitation signal was applied as the Ricker function with a central frequency of 2 GHz. The distance between the transmitting and receiving antenna in the model was set to 6

cm according to the actual distance between the transmitter and receiver in the IDS antenna. The models were discretised using a grid with spatial steps of 0.5 mm × 0.5 mm. For each model, calculations for 15 antenna positions were recorded, moving along the specimen every 10 mm. The zero time of acquired A-scans was defined using the second derivative [43]. Based on the time of the reflected signal, the velocity of electromagnetic waves was determined and then the effective permittivity was calculated as a mean value from 15 A-scans.

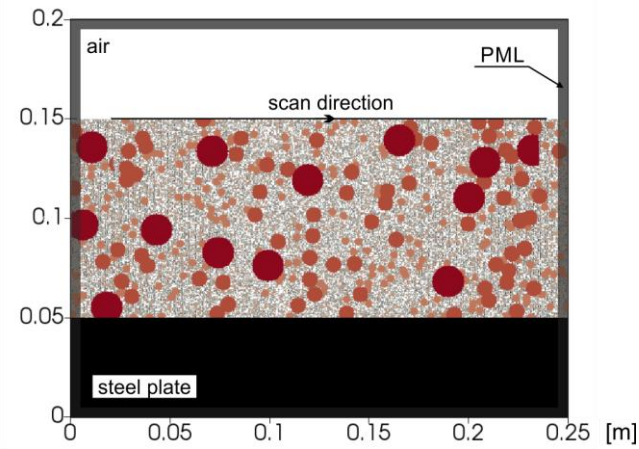

Figure 8. Heterogeneous numerical model of concrete for 0% degree of saturation

In the first stage of the FDTD calculations, the dielectric parameters obtained from the experimental studies were adopted ($\varepsilon_a = 1$, $\varepsilon_w = 79.1$, and $\varepsilon_m = 6.2$). The results are displayed in Figure 7 with red stars. It is clearly visible that the data did not coincide with the experimental data; this is because the calculated effective permeability was close to the weighted average permittivity of the individual phases, where the weighting factor was the volume of a given phase. Next, the adaptation of the numerical model was performed by introducing substitute values of the dielectric permittivity of the solid and liquid phases. The substitute values were obtained using the proposed numerical CRIM (magenta line in Figure 6, according to Eq. (8)) including the weighted average dielectric permittivity. In this manner, the substitute permittivity of water $\varepsilon_{ws} = 40.33$ and the substitute permittivity of the solid phase $\varepsilon_{ms} = 5.83$ were obtained. Moreover, damping was introduced into the model considering the water conductivity as $\sigma = 0.95$ S/m according to Eq. (9). The results of the numerical simulations using the adopted model are displayed in Figure 7 with green diamonds. It can be observed that the adaptation of the FDTD numerical model ensured an acceptable agreement of the numerical results with the measurement data.

3.5. Validation of numerical model

In the last stage, the results of the FDTD calculations for the concrete specimen described in Section 3.1 were compared with the experimental measurements. Two numerical models were created, namely homogeneous and heterogeneous (Figure 9). The models accurately represented the location and size of the reinforcing bars as well as the notch. The external dimensions of the models were 86 cm × 20 cm. The models were discretised using a grid with spatial steps of 0.5 mm × 0.5 mm. Three different degrees of saturation were considered: 0%, 50%, and 100%, which corresponded (according to Eq. (7)) to the following values of dielectric permittivity: $\varepsilon_e = 4.61$ (0% saturation), $\varepsilon_e = 6.46$ (50% saturation), and $\varepsilon_e = 8.62$ (100% saturation). For the homogeneous model (Figure 9a), permittivity values were adopted as above. In the case of the heterogeneous model (Figure 9b), substitute values of the material parameters were set as $\varepsilon_a = 1$, $\varepsilon_{ms} = 5.83$, $\varepsilon_{ws} = 40.33$, and $\sigma = 0.95$ S/m (according to the procedure described in Section 3.4).

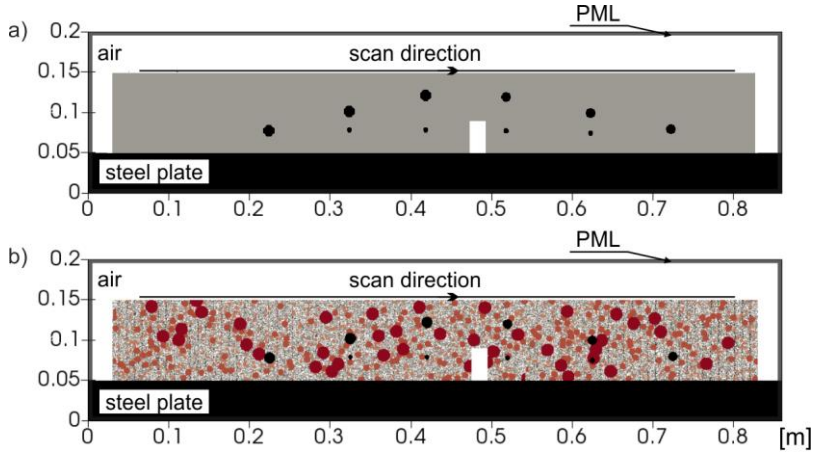

Figure 9. Numerical models of concrete specimen: a) homogeneous and b) heterogeneous

Numerical radargrams obtained using both homogenous and heterogeneous models were compared with the experimental data as displayed in Figures 9, 10, and 11. Figure 10 displays the GPR maps for the specimen with a degree of saturation of 0%. It can be observed that the GPR map calculated for the heterogeneous model (Figure 10c) is considerably more similar to the experimental model (Figure 10a) than the radargram calculated for the homogeneous model (Figure 10b). The radargram calculated for the heterogeneous model revealed numerous reflections, especially visible in the area of the unreinforced concrete, which did not appear on the map from the homogeneous model.

Figure 10 displays the results of the calculations and experiments for the specimen with a degree of saturation of 50%. In this case, again, the map for the heterogeneous model (Figure 11c) is considerably more similar to the experimental data (Figure 11a) compared to the

homogeneous model (Figure 11b). There is also a decrease in the amplitude of the reflection signal from the steel rods. Figure 12 displays the GPR maps for a 100% saturation sample, where the largest differences between the homogeneous (Figure 12b) and heterogeneous models (Figure 12c) were revealed; these are due to the high water content in the pores of the concrete. There is a significant drop in the amplitude of the wave reflection, which is consistent with the experimental data (Figure 12a).

Then, the experimental and numerical maps were analysed in terms of the possibility of detecting the notch in the investigated specimen. It was observed that in the sample containing several reinforcing bars at different levels, the identification of the notch at the lower part of the specimen was not unambiguously possible, regardless of the degree of saturation of concrete.

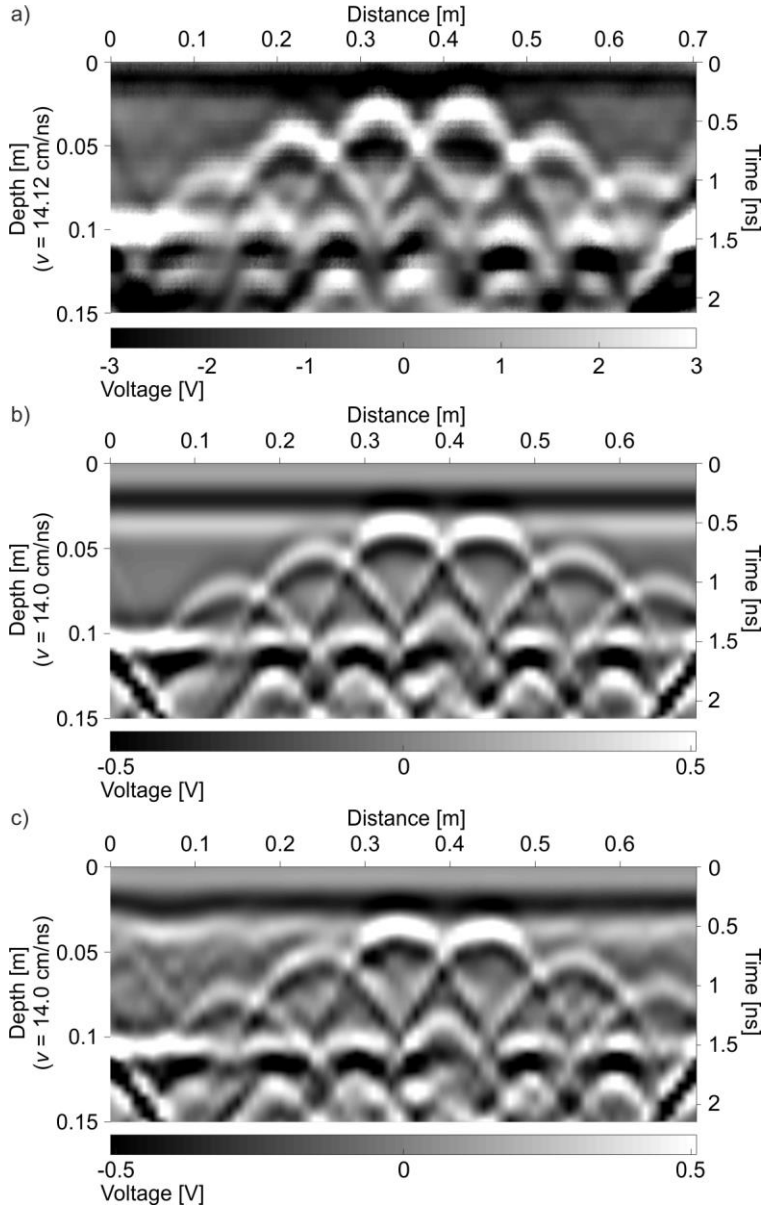

Figure 10. GPR maps for concrete specimen with 0% saturation degree: a) experimental results, b) homogeneous model results, and c) heterogeneous model results

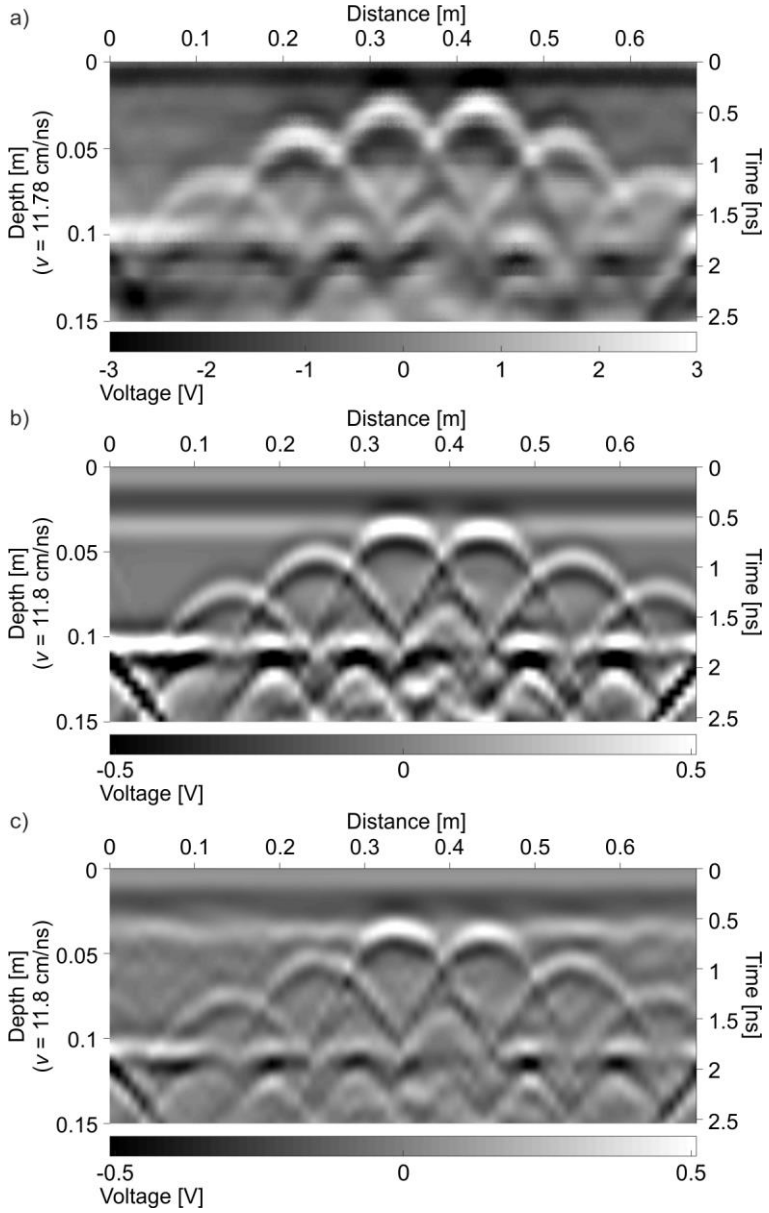

Figure 11. GPR maps for concrete specimen with 50% saturation degree: a) experimental results, b) homogeneous model results, and c) heterogeneous model results

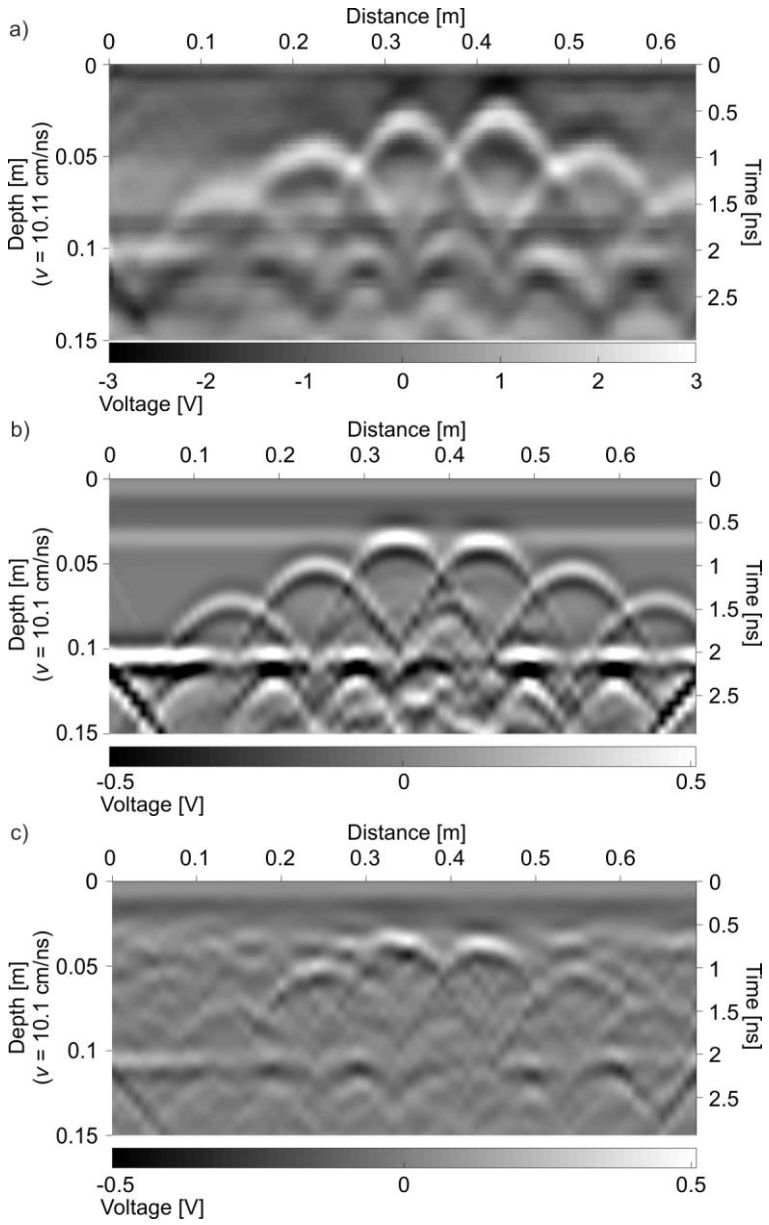

Figure 12. GPR maps for concrete specimen with 100% saturation degree: a) experimental results, b) homogeneous model results, and c) heterogeneous model results

4. GPR investigations on reinforced concrete bridge

4.1. Description of structure

The object of the investigations was a frame pedestrian bridge, a part of the Pomeranian Metropolitan Railway station in Gdańsk, Poland. A reinforced concrete slab with a thickness of 50 cm and a width of 371 cm was monolithically connected to the columns. Figure 13 displays a view of the bridge during construction and a reinforcement drawing based on the technical documentation. Dehydration was designed as linear sewage situated in the bridge axis (Figure 14). The tested structure was chosen because it enabled conducting measurements at two stages, representing different levels of concrete moisture.

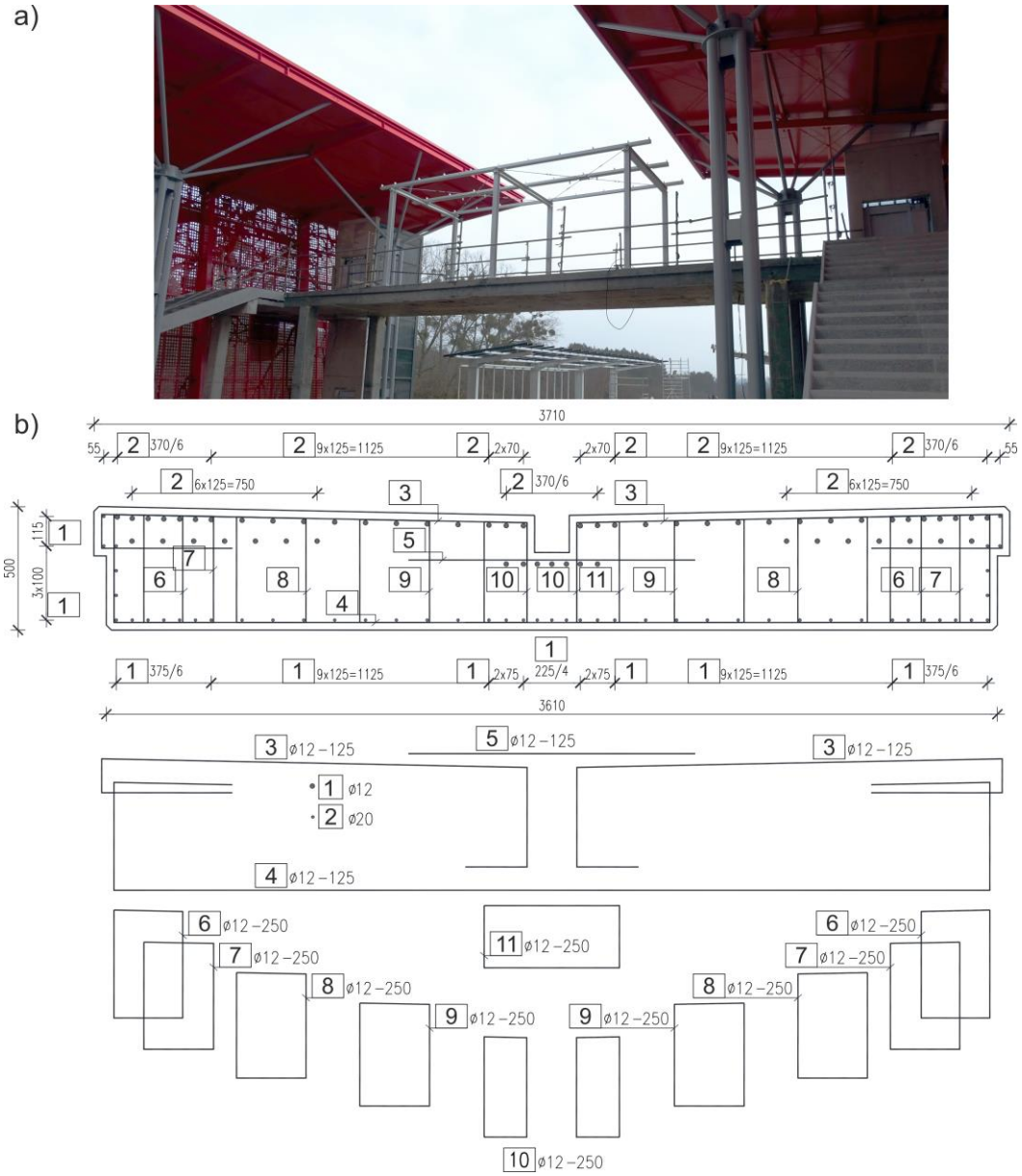

Figure 13. Reinforced concrete footbridge (Gdańsk, Poland, 54°21’19.0”N 18°31’44.2”E): a) general view and b) supporting cross section of bridge with reinforcement drawing

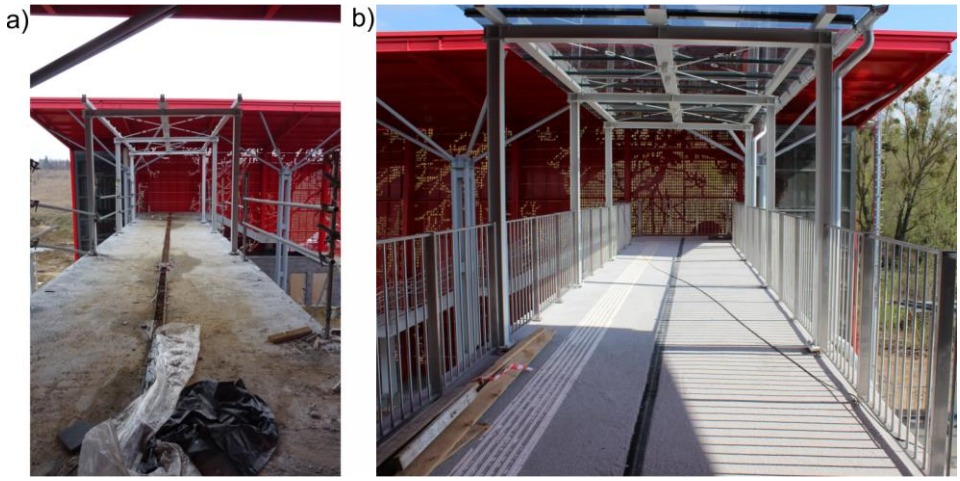

Figure 14. View on bridge deck: a) during construction (Survey #1) and b) two months later (Survey #2)

4.2. GPR surveys

The bridge object was experimentally tested to analyse the influence of the water contained in the concrete on the GPR results. GPR surveys were performed in two stages. The first measurements were conducted during the construction of the bridge (Survey #1, Figure 14a) when the concrete moisture was at a high level. In fact, immediately before the tests, significant precipitation occurred, increasing the degree of saturation. The second GPR surveys were conducted two months later (Survey #2, Figure 14b) when the surface of the pedestrian bridge was complete.

During the GPR inspections, radargrams were acquired along different longitudinal profiles (Figure 15). The registered signals had a length of 32 ns, and the number of recorded samples was 1024 with a step distance of 10 mm.

Figure 15. Bridge deck during GPR measurements (Survey #2)

4.3. Identification of material properties

The material constants of the concrete were determined based on an estimation of the propagation velocity of the electromagnetic wave. Owing to the lack of reflection from the bottom of the reinforced concrete slab, the velocity of the wave was estimated using the hyperbola fitting method. The procedure was conducted on two B-scans from the longitudinal profiling, which were acquired on two different measurement dates. For each map, points on the four hyperbolas were extracted. Next, the approximation process was applied using the Levenberg–Marquardt method [41] and the model of diffraction hyperbola considering the actual bar radius and distance between the transmitting and receiving antennas [9]. Figure 16 presents the GPR maps with marked extracted points and fitted hyperbolas. The velocity was averaged from four hyperbolas. Its identified value was v = 10.8 cm/ns (for Survey #1) and

v = 12.5 cm/ns (for Survey #2), which according to Eq. (6), enabled calculation of the permittivity values $\varepsilon_e = 7.72$ and $\varepsilon_e = 5.76$.

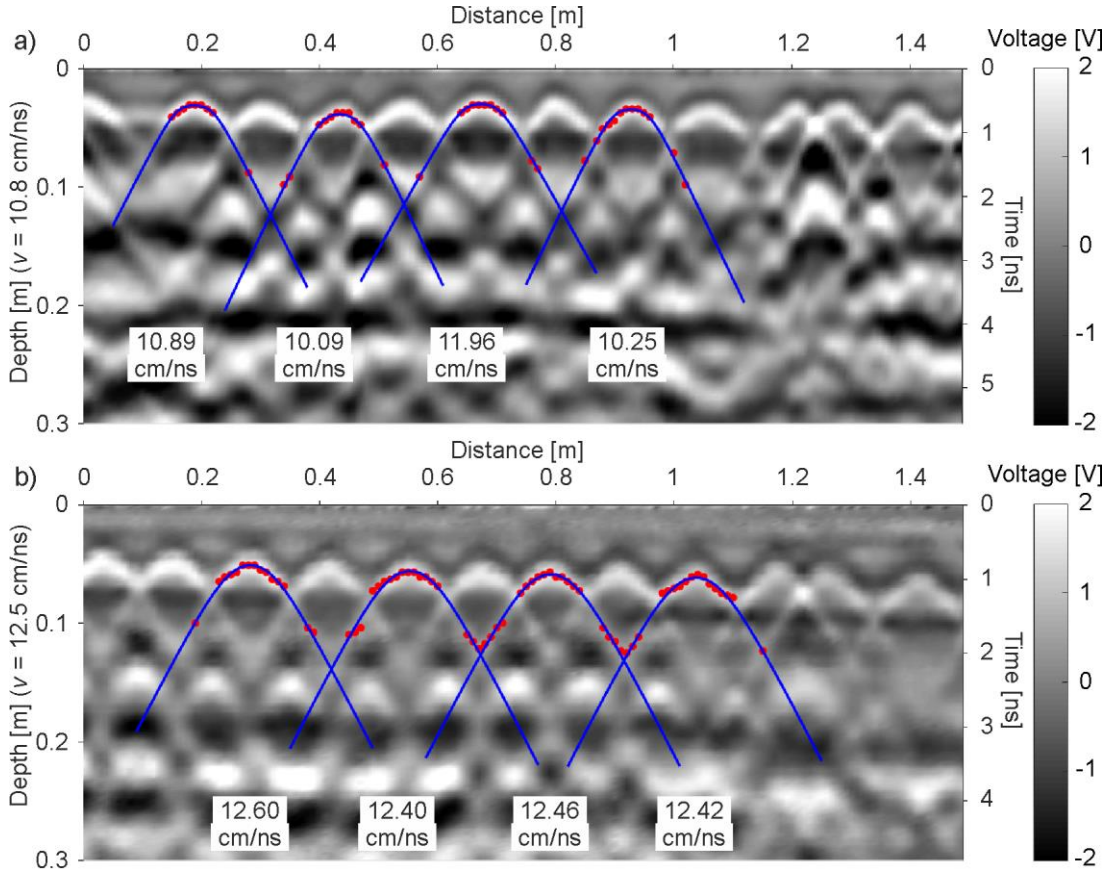

Figure 16. Experimental GPR maps with extracted points and approximated hyperbolas: a) Survey #1 and b) Survey #2

4.4. Determination of substitute values of material properties for numerical modelling

The determination of the substitute values of the dielectric parameters was performed assuming that for the tested bridge, the porosity of the concrete was 20% and volumetric absorption was 10%. As mentioned in Section 2, such fixed assumptions could influence the accuracy of the model. Based on the experimentally identified values of the dielectric permittivity during the two GPR surveys, the modified CRIM was applied according to Eq. (7). The material constants of the liquid and gas phases were assumed as known ($\varepsilon_a = 1$, $\varepsilon_w = 79.1 + i8.6$) and using the nonlinear curve fitting process (blue line in Figure 17), the dielectric permittivity for the solid phase was identified as $\varepsilon_m = 5.46$.

Next, the proposed numerical CRIM was applied according to Eq. (8) to calculate the substitute values of the dielectric permittivity of the liquid and solid phases. The nonlinear fitting process (magenta line in Figure 17) was conducted enabling the identification of the

substitute permittivity of the water as $\varepsilon_{ws} = 39.86$ and substitute permittivity of the solid phase as $\varepsilon_{ms} = 5.46$. The water conductivity was set as $\sigma = 0.95$ S/m according to Eq. (9).

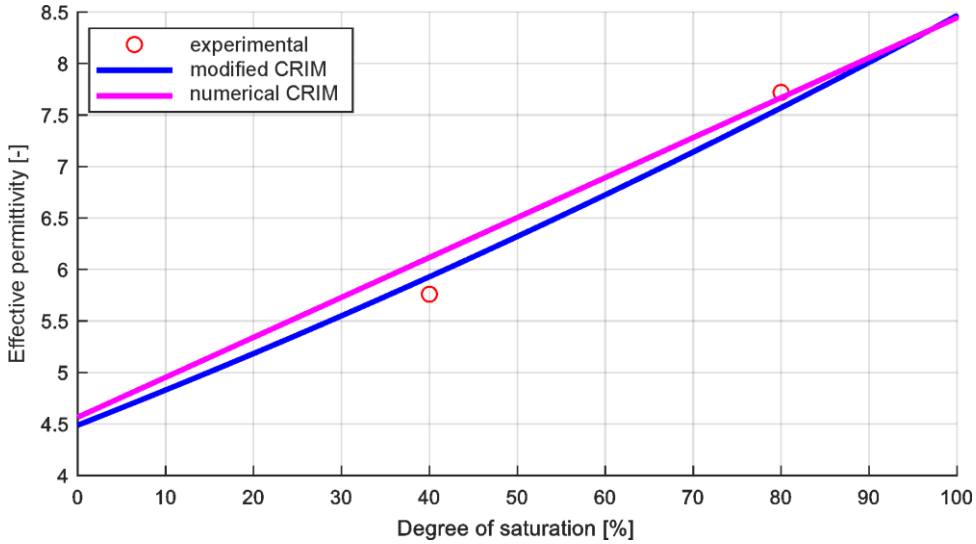

Figure 17. Relationship between effective permittivity and degree of saturation for tested bridge

4.5. FDTD modelling

Numerical analyses of the electromagnetic wave propagation were conducted for longitudinal profiling and compared with the measurement data. A part of the bridge deck with a length of 1.6 m was selected for the calculations (Figure 18). Four numerical models were prepared. Two included the homogenous concrete model for Surveys #1 and #2. The models modified the values of the dielectric permittivity ($\varepsilon_e = 7.72$ for Survey #1 and $\varepsilon_e = 5.76$ for Survey #2). The other two FDTD models utilised the proposed heterogeneous model of concrete. They were defined using the same material constants ($\varepsilon_a = 1$, $\varepsilon_{ws} = 39.86$, $\varepsilon_{ms} = 5.46$, and $\sigma = 0.95$ S/m), differing only in the water content in the concrete mix.

The FDTD calculations were conducted using gprMax software. An excitation was applied as the Ricker function with a central frequency of 2 GHz. The distance between the transmitting and receiving antenna was 6 cm. The 2-D model had external dimensions of 1.6 m × 0.6 m and was divided into Yee cells with a size of 0.5 mm. At the edges of the FDTD model, perfectly matched layer (PML) absorbing boundary conditions were set up.

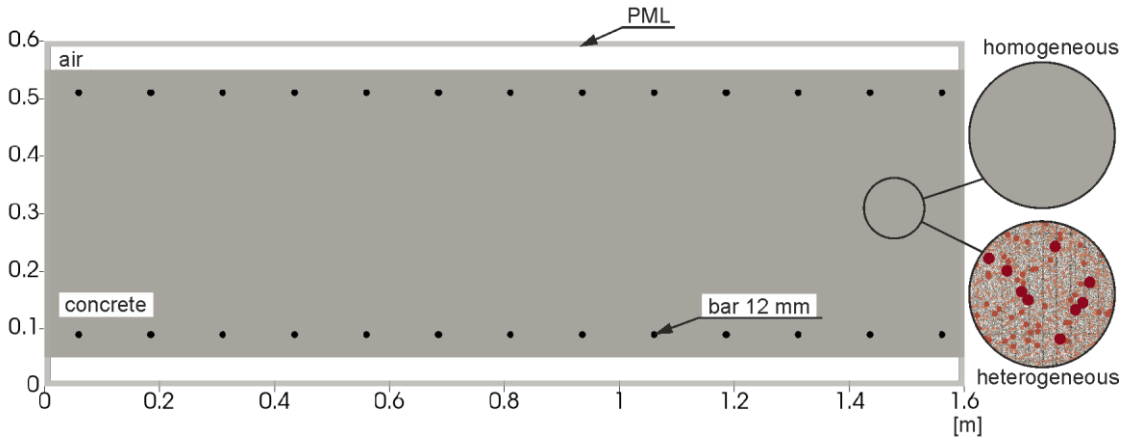

Figure 18. Numerical models of part of reinforced concrete slab for longitudinal profile

4.6. Analysis of results

Figure 19 displays a comparison of the experimental and numerical B-scans acquired along the longitudinal profile. It can be observed that the GPR maps with a fixed depth axis for Surveys #1 and #2 differed in the time axis owing to the different values of the dielectric permittivity of the concrete.

The results of the *in situ* surveys (Figure 19a) enabled the identification of the upper reinforcing bars; however, the lower layer of bars, as well as the bottom of the deck, could not be detected. The GPR maps calculated using the homogeneous model are displayed in (Figure 19b). Regular and strong diffraction hyperbolas indicating the upper and lower row of reinforcing bars are visible. Moreover, a linear reflection at a depth of 0.5 is visible, indicating the bottom of the deck.

Figure 19c presents the numerical GPR maps for the heterogeneous model with varying degrees of saturation. The model with 80% saturation (Survey #1) revealed clear reflections from the upper bars. However, because of the strong damping properties of the water, below this layer of bars, the amplitude of the reflected signal significantly decreased. Conversely, on the GPR map calculated for a model including a 40% saturation level (Survey #2), the reflections from the bottom part of the bridge deck can be observed. Moreover, the concrete area revealed many reflections, from individual concrete fractions, as in the experimental GPR maps.

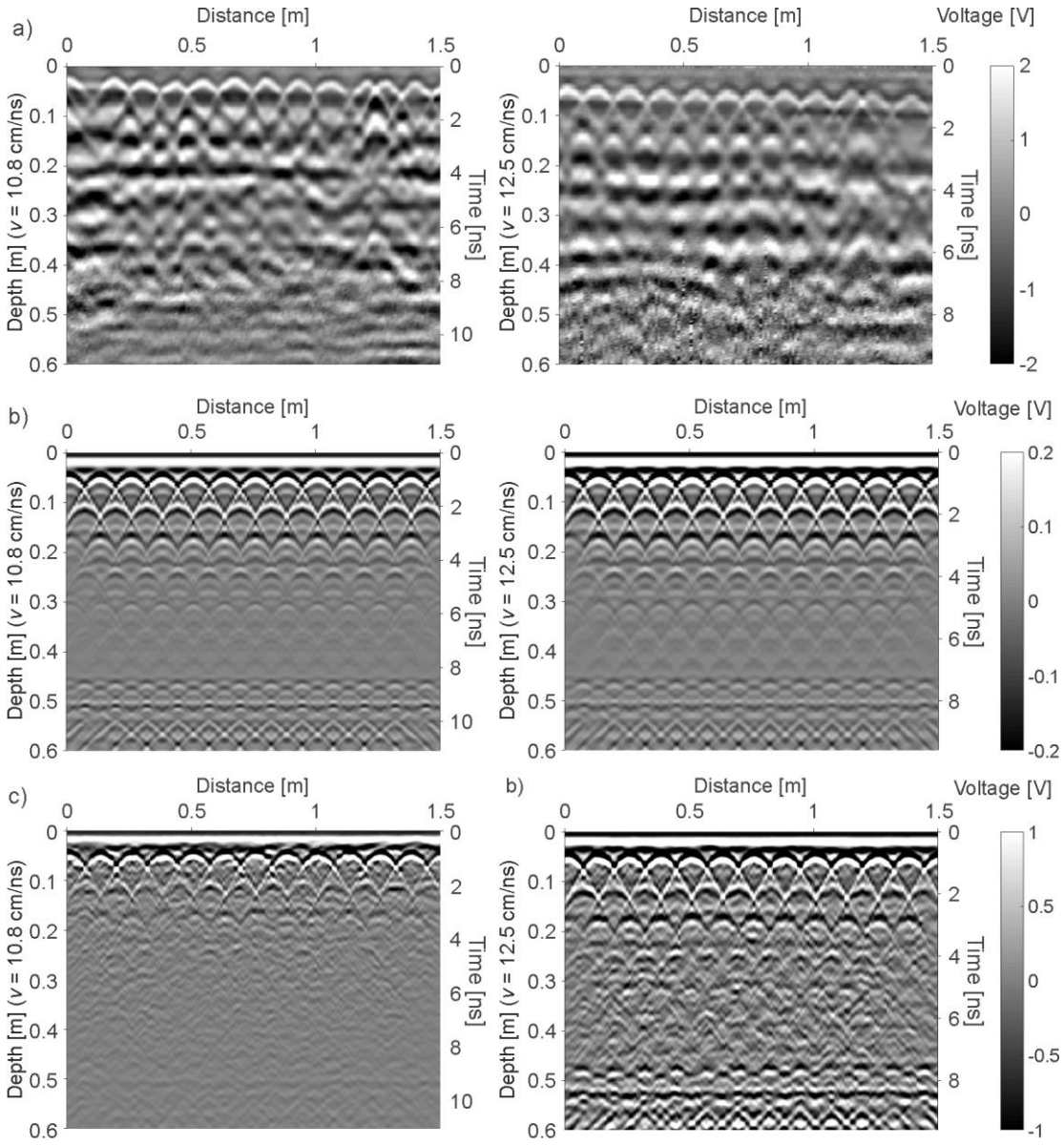

Figure 19. GPR maps for tested bridge (1st column – Survey #1 and 2nd column – Survey #2): a) experimental results, b) homogeneous model results, and c) heterogeneous model results

5. Conclusions

In this study, we demonstrated the importance of realistic FDTD modelling of concrete for ground penetrating radar diagnostics of civil engineering structures with changing water content. The following conclusions can be formulated:

1. The moisture contained in the tested concrete structure had a strong influence on the results of the GPR surveys. High water content caused a significant decrease in the radar wave velocity owing to the strong attenuation of the waves and influenced the possibility of detecting reinforcing bars or potential damage to the concrete.
2. It was proven that changes in dielectric permittivity depending on the degree of saturation should be described using the modified CRIM to consider the fact that not all air pores contained in the concrete must be filled with water.
3. It was revealed that for proper FDTD simulations, determination of the substitute material parameters is necessary, according to the proposed numerical CRIM.
4. The developed heterogeneous model of concrete could simulate in situ GPR signals more accurately than the standard homogeneous model.
5. The model proposed in this paper is expected to be particularly useful in the inspection of concrete structures with a changing level of saturation, or for monitoring concrete maturity in structures during the early stages of hydration.

References

1. Wai-Lok Lai, W.; Dérobert, X.; Annan, P. A review of Ground Penetrating Radar application in civil engineering: A 30-year journey from Locating and Testing to Imaging and Diagnosis. *NDT E Int.* **2018**, *96*, 58–78, doi:10.1016/j.ndteint.2017.04.002.
2. McCann, D. M.; Forde, M. C. Review of NDT methods in the assessment of concrete and masonry structures. *NDT E Int.* **2001**, *34*, 71–84, doi:10.1016/S0963-8695(00)00032-3.
3. Bęben, D.; Mordak, A.; Anigacz, W. Identification of viaduct beam parameters using the Ground Penetrating Radar (GPR) technique. *NDT E Int.* **2012**, *49*, 18–26, doi:10.1016/j.ndteint.2012.03.001.
4. Clem, D. J.; Schumacher, T.; Deshon, J. P. A consistent approach for processing and interpretation of data from concrete bridge members collected with a hand-held GPR device. *Constr. Build. Mater.* **2015**, *86*, 140–148, doi:10.1016/j.conbuildmat.2015.03.105.
5. Lachowicz, J.; Rucka, M. Application of GPR method in diagnostics of reinforced concrete structures. *Diagnostyka* **2015**, *16*, 31–36.
6. Chang, C. W.; Lin, C. H.; Lien, H. S. Measurement radius of reinforcing steel bar in concrete using digital image GPR. *Constr. Build. Mater.* **2009**, *23*, 1057–1063, doi:10.1016/j.conbuildmat.2008.05.018.
7. Zanzi, L.; Arosio, D. Sensitivity and accuracy in rebar diameter measurements from dual-polarized GPR data. *Constr. Build. Mater.* **2013**, *48*, 1293–1301, doi:10.1016/j.conbuildmat.2013.05.009.
8. Pérez-Gracia, V.; González-Drigo, R.; Di Capua, D. Horizontal resolution in a non-destructive shallow GPR survey: An experimental evaluation. *NDT E Int.* **2008**, *41*, 611–620, doi:10.1016/j.ndteint.2008.06.002.
9. Lachowicz, J.; Rucka, M. 3-D finite-difference time-domain modelling of ground penetrating radar for identification of rebars in complex reinforced concrete structures. *Arch. Civ. Mech. Eng.* **2018**, *18*, 1228–1240, doi:https://doi.org/10.1016/j.acme.2018.01.010.
10. Hong, S.; Lai, W. L.; Wilsch, G.; Helmerich, R.; Helmerich, R.; Günther, T.; Wiggenhauser, H. Periodic mapping of reinforcement corrosion in intrusive chloride contaminated concrete with GPR. *Constr. Build. Mater.* **2014**, *66*, 671–684,

doi:10.1016/j.conbuildmat.2014.06.019.

11. Ma, X.; Liu, H.; Wang, M. L.; Birken, R. Automatic detection of steel rebar in bridge decks from ground penetrating radar data. *J. Appl. Geophys.* **2018**, *158*, 93–102, doi:10.1016/j.jappgeo.2018.07.010.
12. Mertens, L.; Persico, R.; Matera, L.; Lambot, S. Automated detection of reflection hyperbolas in complex GPR images with no a priori knowledge on the medium. *IEEE Trans. Geosci. Remote Sens.* **2016**, *54*, 580–596, doi:10.1109/TGRS.2015.2462727.
13. Wiwatrojanagul, P.; Sahamitmongkol, R.; Tangtermsirikul, S.; Khamsemanan, N. A new method to determine locations of rebars and estimate cover thickness of RC structures using GPR data. *Constr. Build. Mater.* **2017**, *140*, 257–273, doi:10.1016/j.conbuildmat.2017.02.126.
14. Al-Nuaimy, W.; Shihab, S.; Eriksen, A. Data fusion for accurate characterisation of buried cylindrical objects using GPR. In *Proceedings of the Tenth International Conference on Ground Penetrating Radar*; Delft, 2004; Vol. 1, pp. 359–362.
15. Shihab, S.; Al-Nuaimy, W. Radius estimation for cylindrical objects detected by ground penetrating radar. *Subsurf. Sens. Technol. Appl.* **2005**, *6*, 151–166, doi:10.1007/s11220-005-0004-1.
16. Ristic, A. V.; Petrovacki, D.; Govedarica, M. A new method to simultaneously estimate the radius of a cylindrical object and the wave propagation velocity from GPR data. *Comput. Geosci.* **2009**, *35*, 1620–1630, doi:10.1016/j.cageo.2009.01.003.
17. Mechbal, Z.; Khamlichi, A. Determination of concrete rebars characteristics by enhanced post-processing of GPR scan raw data. *NDT E Int.* **2017**, *89*, 30–39, doi:10.1016/j.ndteint.2017.03.005.
18. Sagnard, F.; Tarel, J.-P. Template-matching based detection of hyperbolas in ground-penetrating radargrams for buried utilities. *J. Geophys. Eng.* **2016**, *13*, 491–504, doi:10.1088/1742-2132/13/4/491.
19. Sham, J. F. C.; Lai, W. W. L. Development of a new algorithm for accurate estimation of GPR's wave propagation velocity by common-offset survey method. *NDT E Int.* **2016**, *83*, 104–113, doi:10.1016/j.ndteint.2016.05.002.
20. Yehia, S.; Qaddoumi, N.; Farrag, S.; Hamzeh, L. Investigation of concrete mix variations and environmental conditions on defect detection ability using GPR. *NDT E Int.* **2014**, *65*, 35–46, doi:10.1016/j.ndteint.2014.03.006.
21. Robert, A. Dielectric permittivity of concrete between 50 MHz and 1 GHz and GPR measurements for building materials evaluation. *J. Appl. Geophys.* **1998**, *40*, 89–94,

doi:10.1016/S0926-9851(98)00009-3.

22. Laurens, S.; Balayssac, J. P.; Rhazi, J.; Klysz, G.; Arliguie, G. Non-destructive evaluation of concrete moisture by GPR: experimental study and direct modeling. *Mater. Struct.* **2005**, *38*, 827–832, doi:10.1617/14295.
23. Klysz, G.; Balayssac, J. Determination of volumetric water content of concrete using ground-penetrating radar. **2007**, *37*, 1164–1171, doi:10.1016/j.cemconres.2007.04.010.
24. Agred, K.; Klysz, G.; Balayssac, J. Location of reinforcement and moisture assessment in reinforced concrete with a double receiver GPR antenna. *Constr. Build. Mater.* **2018**, *188*, 1119–1127, doi:10.1016/j.conbuildmat.2018.08.190.
25. Kaplanvural, I.; Peksen, E.; Özkap, K. Volumetric water content estimation of C-30 concrete using GPR. *Constr. Build. Mater. J.* **2018**, *166*, 141–146, doi:10.1016/j.conbuildmat.2018.01.132.
26. Lai, W. L.; Kou, S. C.; Tsang, W. F.; Poon, C. S. Characterization of concrete properties from dielectric properties using ground penetrating radar. *Cem. Concr. Res.* **2009**, *39*, 687–695, doi:10.1016/j.cemconres.2009.05.004.
27. Lo Monte, F.; Lombardi, F.; Felicetti, R.; Lualdi, M. Ground-Penetrating Radar monitoring of concrete at high temperature. *Constr. Build. Mater.* **2017**, *151*, 881–888, doi:10.1016/j.conbuildmat.2017.06.114.
28. Shen, P.; Liu, Z. Study on the hydration of young concrete based on dielectric property measurement. *Constr. Build. Mater.* **2019**, *196*, 354–361, doi:10.1016/j.conbuildmat.2018.11.150.
29. Xie, X.; Qin, H.; Yu, C.; Liu, L. An automatic recognition algorithm for GPR images of RC structure voids. *J. Appl. Geophys.* **2013**, *99*, 125–134, doi:10.1016/j.jappgeo.2013.02.016.
30. Xiang, L.; Zhou, H.-L.; Shu, Z.; Tan, S.-H.; Liang, G.-Q.; Zhu, J. GPR evaluation of the Damaoshan highway tunnel: A case study. *NDT E Int.* **2013**, *59*, 68–76, doi:10.1016/j.ndteint.2013.05.004.
31. Lachowicz, J.; Rucka, M. Numerical modeling of GPR field in damage detection of a reinforced concrete footbridge. *Diagnostyka* **2016**, *17*, 3–8.
32. Solla, M.; González-Jorge, H.; Álvarez, M. X.; Arias, P. Application of non-destructive geomatic techniques and FDTD modeling to metrical analysis of stone blocks in a masonry wall. *Constr. Build. Mater.* **2012**, *36*, 14–19, doi:10.1016/j.conbuildmat.2012.04.134.
33. Diamanti, N.; Giannopoulos, A.; Forde, M. C. Numerical modelling and experimental

verification of GPR to investigate ring separation in brick masonry arch bridges. *NDT E Int.* **2008**, *41*, 354–363, doi:10.1016/j.ndteint.2008.01.006.

34. Rucka, M.; Lachowicz, J.; Zielińska, M. GPR investigation of the strengthening system of a historic masonry tower. *J. Appl. Geophys.* **2016**, *131*, 94–102, doi:10.1016/j.jappgeo.2016.05.014.
35. Gürel, L.; Oguz, U. Simulations of Ground-Penetrating Radars Over Lossy and Heterogeneous Grounds. *IEEE Trans. Geosci. Remote Sens.* **2001**, *39*, 1190–1197.
36. Giannakis, I.; Giannopoulos, A.; Warren, C. A realistic FDTD numerical modeling framework of ground penetrating radar for landmine detection. *IEEE J. Sel. Top. Appl. Earth Obs. Remote Sens.* **2015**, *9*, 37–51, doi:10.1109/JSTARS.2015.2468597.
37. Halabe, U.; Maser, K.; Kausel, E. Propagation characteristics of electromagnetic waves in concrete. *Tech. Rep. AD-A207387, Cambridge Dep. Civ. Eng. MIT* **1989**, 1–106.
38. Warren, C.; Giannopoulos, A.; Giannakis, I. An advanced GPR modelling framework: The next generation of gprMax. In *8th International Workshop on Advanced Ground Penetrating Radar (IWAGPR)*; Florence, 2015; pp. 1–4.
39. Warren, C.; Giannopoulos, A.; Giannakis, I. gprMax: Open source software to simulate electromagnetic wave propagation for Ground Penetrating Radar. *Comput. Phys. Commun.* **2016**, *209*, 163–170, doi:10.1016/j.cpc.2016.08.020.
40. Luebbers, R.; Hunsberger, F. P.; Kunz, K. S.; Standler, R. B.; Schneider, M. A frequency-dependent finite-difference time-domain formulation for dispersive materials. *IEEE Trans. Electromagn. Compat.* **1990**, *32*, 222–227.
41. Marquardt, D. W. An algorithm for least-squares estimation of nonlinear parameters. *J. Soc. Ind. Appl. Math.* **1963**, *11*, 431–441.
42. Giannopoulos, A. Modelling ground penetrating radar by GprMax. *Constr. Build. Mater.* **2005**, *19*, 755–762, doi:10.1016/j.conbuildmat.2005.06.007.
43. Lai, W. L.; Kind, T.; Wiggenhauser, H. A Study of Concrete Hydration and Dielectric Relaxation Mechanism Using Ground Penetrating Radar and Short-Time Fourier Transform. *EURASIP J. Adv. Signal Process.* **2010**, 317216, doi:10.1155/2010/317216.